Check for updates

# Toward understanding and development of the three-dimensional atomic structures of supported metal catalysts

Junya Ohyama [ID] [ab]

Understanding of supported metal catalysts, which are indispensable for numerous practical chemical processes including chemical production, environmental purification, and power generation, has deepened alongside advances in analytical techniques. In particular, recent progress in direct atomic-scale and even three-dimensional analysis techniques has revealed that actual structures often differ significantly from conventionally assumed model structures, leading to remarkable catalysis. In this review, our recent studies on supported metal catalysts using such advanced analytical techniques, specifically high-energy-resolution fluorescence-detected X-ray absorption near edge structure (HERFD-XANES) and spherical aberration-corrected scanning transmission electron microscopy (Cs-STEM), are reviewed. First, the complementarity of X-ray absorption fine structure spectroscopy (XAFS) and STEM in characterizing the diverse structures of supported catalysts is described. Representative examples of distinctive catalyst structures and their associated catalytic properties revealed using HERFD-XANES and Cs-STEM are then presented. Finally, the three-dimensional atomic structure of a practical supported metal nanoparticle catalyst, resolved for the first time through the application of atomic-resolution electron tomography, is discussed, and future directions in supported metal catalyst research enabled by 3D structural analysis are explored.

[a] *Faculty of Advanced Science and Technology, Kumamoto University, 2-39-1 Kurokami, Chuo-ku, Kumamoto 860-8555, Japan. E-mail: ohyama@kumamoto-u.ac.jp*
[b] *Institute of Industrial Nanomaterials (IINa), Kumamoto University, 2-39-1 Kurokami, Chuo-ku, Kumamoto 860-8555, Japan*

*Junya Ohyama received his PhD degree in engineering from Kyoto University in 2011. He then joined the Graduate School of Engineering at Nagoya University as an assistant professor. In 2018, he joined the Faculty of Advanced Science and Technology at Kumamoto University as an associate professor. His current research interests focus on designing and developing solid catalyst structures through the understanding of structure–performance relationships for applications in fuel cells, methane conversion, and exhaust gas purification.*

**Junya Ohyama**

## 1. Introduction

The structure of solid catalysts is a key determinant of their catalytic performance.[1,2] Unlike idealized model surfaces and bulk structures, practical solid catalysts exhibit complex structural features such as diverse crystal facets, steps, corners, edges, atomic distortions, crystal and lattice defects, and interfaces between dissimilar components such as metal–support interfaces. These intricate structural variations significantly influence their catalysis. However, accurately describing these structures is extremely challenging, and many aspects of their role in catalysis are not yet fully understood. In contrast, molecular catalysts in organic and inorganic chemistry have become highly sophisticated, owing to the atomic-level understanding of their three-dimensional (3D) structures. This contrast highlights the importance of achieving atomic-level 3D structural characterization for solid catalysts as a key to future advances in the field. Moreover, the visualization of 3D atomic structures enables their digitization, which in turn is expected to advance the digital transformation of catalyst research, ultimately driving innovation in the field of solid catalyst.

Supported metal catalysts are indispensable materials in chemical processes, environmental purification, and power generation, and they will play a crucial role in achieving a
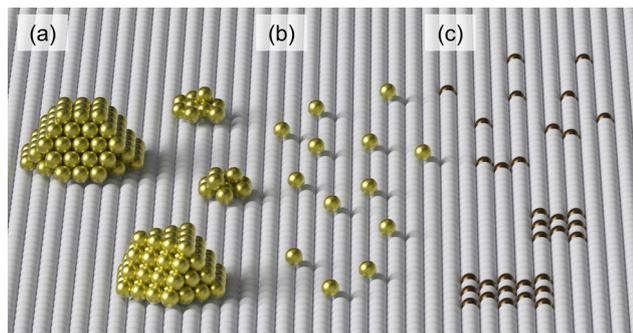
**Fig. 1** Schematic illustration of representative structures of supported metal catalysts: (a) nanoparticles and clusters, (b) atomically dispersed single metal atoms, and (c) incorporated metal atoms and complex metal oxides.

decarbonized society. When the metal species in supported catalysts are reduced to the nanoscale or below, they often exhibit distinctive catalytic properties compared with those of their bulk counterparts.[1] Furthermore, their catalytic performance is highly sensitive to structural variations.[2] A schematic representation of supported metal catalysts is shown in Fig. 1. Metal species can exist on supports in various structural forms, such as nanoparticles, clusters, or isolated single atoms. Depending on the choice of support material and preparation conditions, they may also be incorporated into the support or form complex metal oxides. In the case of clusters and nanoparticles, interactions with the support can induce changes in crystallinity and morphology. Importantly, the catalytic performance of supported metal catalysts is greatly influenced by these structural features. In particular, the local structures of active surface sites, which are on the same spatial scale as the reactant molecules, play a critical role in determining catalytic activity. Therefore, identifying these local surface structures and elucidating their relationship to catalytic performance are essential for a clear understanding of supported metal catalysts. Although such characterization has long been challenging due to the inherent structural complexity of practical supported metal catalysts, recent advances in analytical techniques have made it possible to resolve these 3D structures with atomic-scale resolution.[3–12]

Among the various analytical techniques used to investigate the local structures of solid catalysts, X-ray absorption fine structure (XAFS) spectroscopy is particularly valuable. Recently, high-energy-resolution fluorescence-detected X-ray absorption near edge structure (HERFD-XANES) spectroscopy, which enhances the energy resolution of conventional XANES spectroscopy, has attracted increasing attention.[13–16] Since XAFS reflects the local atomic structure surrounding the element of interest, the improvements in energy resolution means enhancement of spatial resolution, leading to more detailed structural insights. In other words, local structures that were previously indistinguishable can now be resolved and evaluated by HERFD-XANES spectroscopy.

Another major advancement in the structural analysis of solid catalysts is the advent of spherical aberration-corrected scanning transmission electron microscopy (Cs-STEM). With this innovation, the spatial resolution of STEM has improved to below 0.1 nm, enabling the direct observation of single atoms on supports and the determination of atomic positions within clusters and nanoparticles.[17–19] Although Cs-STEM was only commercialized in 2009, it is already becoming a standard tool for catalyst characterization.

Against this background, we have applied these advanced analytical techniques in the study of supported metal catalysts, gaining new insights into their structural effects in hydrocarbon and biomass conversion, energy conversion, and environmental processes. These efforts have led to the development of highly active catalysts and the proposal of sophisticated strategies for catalyst design. In this review, the complementarity of XAFS and STEM in analyzing various structures of supported catalysts is first discussed. Then, the studies we have conducted on catalyst structures and structure–performance relationships using HERFD-XANES and Cs-STEM are presented. Finally, future directions in supported metal catalyst research enabled by 3D structural analysis are explored.

## 2. Complementarity of XAFS and STEM

Supported metal catalysts can adopt diverse structural forms as illustrated in Fig. 1. In many practical systems, the active metal species are highly dispersed on the support surface. Although X-ray diffraction (XRD) is one the most widely used techniques for structural characterization of solid catalysts, it is primarily effective for materials with long-range structural order, such as bulk crystalline phases and periodic porous frameworks. Consequently, conventional XRD is not suitable for analyzing highly dispersed species such as single atoms or small clusters/nanoparticles. However, this limitation of conventional XRD analysis can be addressed by using grazing incidence XRD (GIXRD) and GI small-angle X-ray scattering (GISAXS). Specifically, GIXRD and GISAXS can be employed to evaluate the crystallinity, lattice strain, orientation, size, and morphology of metal nanoparticles supported on substrates.[20–22] Such analyses, however, require samples to take the form of thin films on flat substrates, *i.e.*, metal nanoparticles deposited on flat support substrates. Therefore, while these techniques provide detailed structural information about well-defined systems, they may not be directly applicable to the analysis of practical supported metal catalysts in powder form. In such cases, techniques that probe local atomic environments of dispersed metal species on fine powder supports, namely, XAFS spectroscopy and STEM are particularly powerful. The following subsections discuss the complementarity of these two characterization techniques in analyzing various active site structures of supported metal catalysts.

### 2.1. Single-atom and incorporated structures

A model structure of a recently studied supported Fe complex catalyst is illustrated in Fig. 2.[23,24] Such individually dispersed complexes on a support surface can be regarded as single-atom catalysts. In such structures, the local coordination environment

**Fig. 2** Structure of a fourteen-membered macrocyclic Fe complex (Fe-14MR) supported on carbon.[23,24]

around the metal center, specifically, the metal–ligand bond distances, coordination numbers, and structural distortions, has a strong influence on their catalytic performance. Although, as described later, Cs-STEM enables the visualization of isolated metal atoms, it remains challenging to analyze the surrounding local structure. In contrast, XAFS is particularly effective for this purpose. Extended XAFS (EXAFS) spectral analysis provides quantitative information on the type of coordinating atoms, bond distances, and coordination numbers. These structural features are also reflected in the XANES region, which further allows analysis of local distortions around the X-ray absorbing atom. These principles also apply to incorporated structures, where metal species are incorporated into the support to form locally doped or complex oxide structures. Therefore, XAFS is especially powerful for analyzing the local structures of active sites in single-atom and incorporated catalysts.

### 2.2. Nanoparticle and cluster structures

Next, supported metal nanoparticles and clusters, in which surface atoms serve as catalytic active sites, are considered. Commonly assumed structural models for metal nanoparticles and clusters are truncated octahedron and cuboctahedron, which feature edge, corner, and terrace sites, each with a distinct local coordination environment. Moreover, metal atoms located at the interface with the support inevitably exhibit coordination environments that differ from those on the other exposed surfaces. Thus, a variety of local surface structures exist on a supported metal nanoparticle. Although XAFS spectroscopy remains a valuable technique for characterizing metal nanoparticles, the resulting spectra represent an average over all absorbing atoms in the sample. Consequently, XAFS cannot distinguish between surface atoms with different coordination environments and those in the particle bulk. It is also difficult to evaluate the local structure of individual active sites. In such cases, electron microscopy with sufficiently high spatial resolution to resolve individual surface atoms becomes indispensable. In particular, Cs-STEM is highly useful for analysis of metal nanoparticles and clusters, as it can visualize their surface structures at atomic resolution using a finely focused electron beam smaller than 0.1 nm.

Having understood the characteristics and limitations of each analytical method, we have investigated the structures and structure–performance relationships of supported catalysts with various structures. The following sections present structure–performance relationships revealed by HAADF-XANES and

Cs-STEM analysis in catalysts developed for a range of reactions, including fuel cell electrode reactions, methane conversion, biomass conversion, and environmental purification.

## 3. HERFD-XANES study

In conventional XANES spectroscopy, the X-ray absorption due to excitation of core-level electrons is measured. In this process, the spectra are broadened due to the short lifetime of the resulting core hole. In contrast, HERFD-XANES spectroscopy analyzes a specific fluorescence X-ray emission.[13] The hole associated with this emission has a longer lifetime than that of the initial core hole, resulting in reduced spectral broadening. Consequently, HERFD-XANES offers improved energy resolution. Fig. 3 compares the HERFD-XANES and conventional XANES spectra of $Rh_2O_3$.[25] The HERFD-XANES spectrum exhibits sharper edge rises and more defined peak structures. Because X-ray absorption spectra reflect the local structure around the absorbing atom, HERFD-XANES enables the detection of structural features that are blurred or hidden in conventional XANES. Thus, the introduction of HERFD-XANES to catalyst research provides deeper insights into the relationship between active site structure and catalytic performance, and offers a more refined basis for catalyst design. The following subsections present catalyst structures and structure–performance relationships revealed using HERFD-XANES.

### 3.1. Distortion in single-atom catalysts

The development of platinum-free catalysts for the oxygen reduction reaction (ORR) in proton exchange membrane fuel cells (PEMFCs) has attracted considerable interest. Among these, Fe–N–C catalysts synthesized by pyrolyzing mixtures of Fe precursors with nitrogen and carbon sources, such as metal–organic frameworks or polyimides, have demonstrated promising activity.[27–30] Recent detailed structural analyses have revealed the presence of two types of $FeN_4$ sites in Fe–N–C
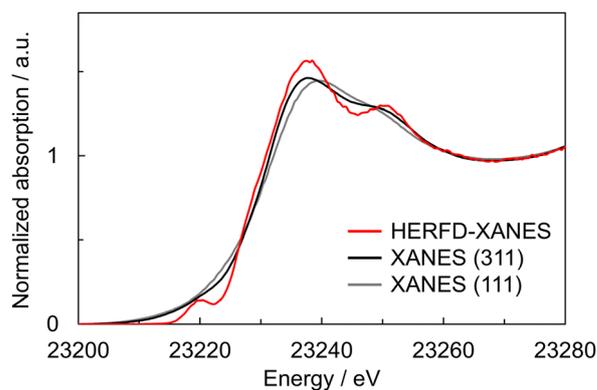


**Fig. 3** Comparison of the Rh K-edge HERFD-XANES spectrum of $Rh_2O_3$ (red line) and conventional XANES spectra of $Rh_2O_3$ measured using Si(111) (gray line) and Si(311) (black line) monochromators. The conventional spectra were taken from the SPring-8 BENTEN database.[26] Reproduced from ref. 25 with permission from the American Chemical Society, copyright 2025.

materials: one embedded in a 16-membered ring and the other in a 14-membered ring.[30] Although the 14-membered ring site is less active than the 16-membered counterpart, it exhibits significantly higher durability and has therefore attracted attention as a practically durable active site. Conventional pyrolysis methods, however, do not permit the controlled synthesis of the 14-membered ring Fe site. To overcome this limitation, a 14-membered macrocyclic Fe complex (Fe-14MR) was synthesized, and carbon supported catalysts (Fe-14MR/C, Fig. 2) were prepared and evaluated for the ORR.[23,24,31] As a result, Fe-14MR/C exhibited much higher durability than a conventional Fe phthalocyanine-based catalyst with the 16-membered ring (Fe-16MR/C). This improvement was attributed to the suppression of Fe dissolution in Fe-14MR/C, resulting from its shorter Fe–N bond length, $i.e.$, stronger Fe–N bonds, compared to Fe-16MR/C. Interestingly, the durability of Fe-14MR/C was further enhanced by heat treatment at 600 °C. However, this enhancement could not be explained by Fe–N bond length, as it remained unchanged after heat treatment. To identify another structural factor contributing to its stability, HERFD-XANES spectroscopy was employed to probe the local coordination environment in greater detail.[24]

Particular attention was directed to the structural distortion around the Fe center. Intuitively, a less distorted coordination environment, in which the Fe atom remains within the plane of the 14-MR ligand, is expected to exhibit greater resistance to leaching. The intensity of the pre-edge peak in Fe K-edge XANES spectra is known to correlate with the degree of distortion around the Fe center. Because this pre-edge feature is inherently weak, HERFD-XANES spectroscopy was employed to capture subtle spectral changes with improved sensitivity. Fig. 4(a) compares the HERFD-XANES and conventional XANES spectra of Fe-14MR/C before heat treatment. The HERFD-XANES spectrum displays a sharper pre-edge feature and a flatter background than the conventional XANES spectrum, enabling more detailed structural analysis from the pre-edge peak. Fig. 4(b) illustrates the relationship between the HERFD-XANES pre-edge peak intensity and the extent of activity loss after electrochemical reaction cycles of heat-treated Fe-14MR/C catalysts. The catalytic degradation diminished as the pre-edge intensity decreased with increasing heat-treatment temperature. The result suggests that reduced structural distortion around the Fe center contributes to the improved durability. Furthermore, our recent results indicate that substituting Fe with Co further reduces the distortion around the active site, markedly enhancing the catalyst stability.[32] These results demonstrate that a more symmetric coordination environment for the active metal center, where the metal atom remains within the plane of the macrocyclic ligand, makes it less susceptible to leaching into the electrolyte, thereby enhancing catalyst durability. Thus, structural symmetry around the active metal center was elucidated as a key factor to the durability of $MN_4$ (M: metal) catalysts.[32] In summary, the HERFD-XANES-based local structural analysis of single-atom catalysts has revealed that the symmetric $MN_4$ structure is crucial for
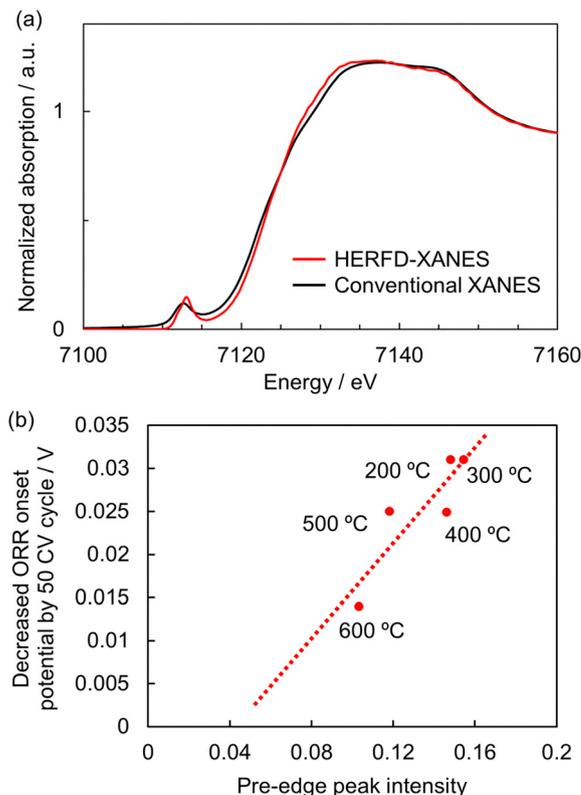


Fig. 4 (a) Fe K-edge HERFD-XANES and conventional XANES spectra of Fe-14MR/C. (b) Decrease in ORR activity after 50 reaction cycles plotted as a function of pre-edge peak intensity. Reproduced from ref. 24 under a CC-BY license. Published by the American Chemical Society.

developing highly durable non-platinum group metal catalysts for fuel cells.

### 3.2. Uncovering incorporated structure

The direct oxidation of methane to methanol and formaldehyde is often described as a "dream reaction" in chemistry due to the challenge of activating stable C–H bond in methane without oxidation of methanol and formaldehyde. However, if this transformation could be achieved with high efficiency, it can dramatically reduce the energy demands currently required for the industrial production of methanol and formaldehyde. Although no catalyst has, to date, achieved the level of activity and selectivity required for the practical implementation of this partial oxidation reaction, previous studies have suggested copper-exchanged zeolites and mixed metal oxides as promising catalyst systems.[33–41] In particular, it has been suggested that catalytic performance is strongly influenced by the local structure of the active site and the characteristics of lattice oxygen formed between different metal species. Building upon these insights, exploring the local structures and lattice oxygen at the metal–support interface is expected to facilitate the development of highly active catalysts.

In supported metal oxide catalysts, diverse lattice oxygen species can form at the interface between the active metal and the oxide support, and in some cases, complex metal oxides

may also be generated depending on specific metal–support combinations (Fig. 1). To systematically investigate these effects, a wide range of supported catalysts with varying compositions was screened.[41] Specifically, 76 supported catalysts were prepared by combining 11 metal oxides (MgO, $Al_2O_3$, $SiO_2$, $TiO_2$, $V_2O_5$, $ZrO_2$, $Nb_2O_5$, $MoO_3$, $Ta_2O_5$, $WO_3$, and $La_2O_3$) as supports with 7 transition metals (V, Mn, Fe, Co, Ni, Cu, and Zn) as supported metals. These 76 supported catalysts and 11 individual metal oxides were evaluated for their performance in the partial oxidation of methane. Among them, $Fe/MoO_3$, $Fe/V_2O_5$, and especially $Fe/Nb_2O_5$ exhibited notably high activity for partial oxidation. To investigate the origin of the high catalytic performance of $Fe/Nb_2O_5$, $Fe/MoO_3$, and $Fe/V_2O_5$, their structures and surface properties were evaluated. However, characterization techniques such as XRD and probe molecule adsorption infrared spectroscopy, which reflect averaged information from both the supported metal species and the support, were not sufficient to identify the structural factors responsible for the differences in catalytic performance. Given the dispersed nature of the supported catalysts, it was necessary to probe the local environment around the active Fe sites. Therefore, HERFD-XANES spectroscopy was employed. Fig. 5 shows the HERFD-XANES spectra of the eleven Fe-based catalysts and their respective catalytic activities. The Fe species in each catalyst exhibited distinct spectral features. Among them, $Fe/Ta_2O_5$, $Fe/WO_3$, $Fe/Al_2O_3$, and $Fe/SiO_2$ displayed spectra closely resembling that of $Fe_2O_3$, indicating that the majority of Fe in these catalysts exists in an $Fe_2O_3$-like structure. These catalysts also consistently showed low selectivity for the methane partial oxidation. In contrast, the remaining seven catalysts exhibited significantly different spectral features compared to $Fe_2O_3$ or FeO. Measurements of reference samples and spectral simulations revealed that the Fe species were incorporated into the supports to form complex metal oxides. This suggests that the formation of complex oxides played a decisive role in the differences in catalytic performance. Very interestingly, all three active catalysts, $Fe/Nb_2O_5$, $Fe/MoO_3$, and $Fe/V_2O_5$, were found to form $ABO_4$-type structures, where A is Fe and B is a group 4–6 transition metal. In addition, although $Fe/WO_3$ primarily formed $Fe_2O_3$, which resulted in low partial oxidation selectivity, $FeWO_4$ synthesized separately exhibited high selectivity for the partial oxidation. Therefore, the screening of supported catalyst structures, in combination with HERFD-XANES analysis of local active-site structures, led to the discovery of $ABO_4$-type structure as a catalyst design for the partial oxidation of methane.

It is worth briefly noting a characteristic of XANES that is relevant to the following discussion. Spectral broadening in XANES, which arises from the finite lifetime of the core hole, becomes more pronounced as the absorption energy of the core-level electron increases.[16] Specifically, in K-edge XANES, elements in the 4th period of the periodic table exhibit broader spectral features than those in the 3rd period (*cf.* Fig. 3 and Fig. 4(a)), due to the shorter lifetime of the 1s core hole. As a result, K-edge XANES spectra of 4th-period elements are often significantly broadened, making it difficult to extract detailed structural information. Therefore, HERFD-XANES offers distinct advantages for structural analysis of materials containing
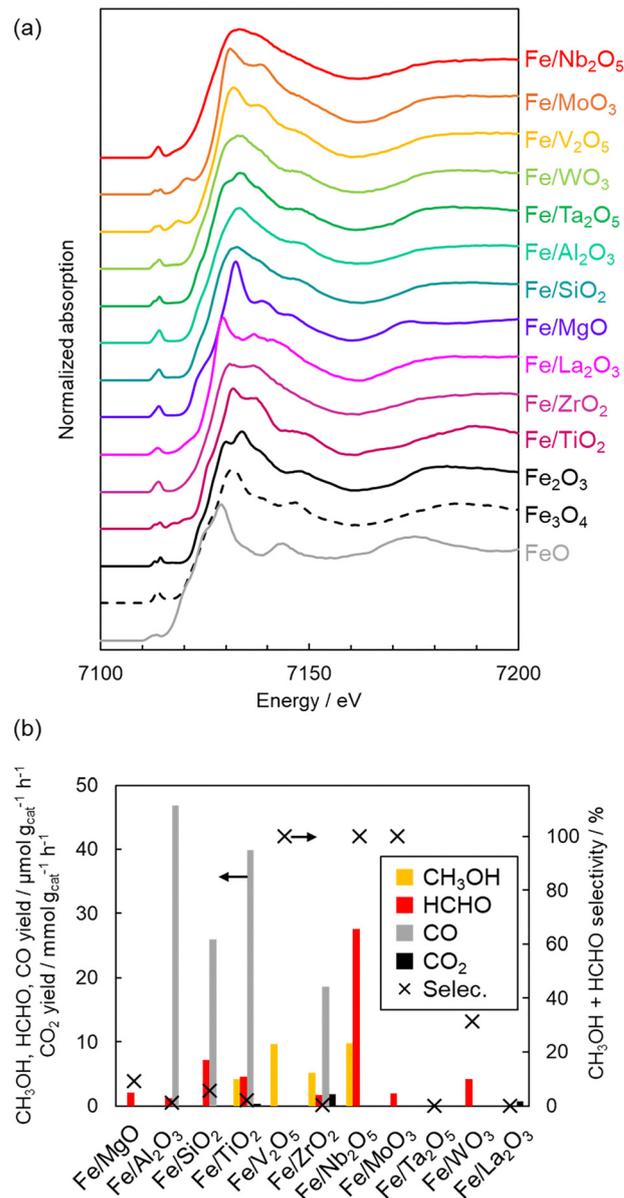


Fig. 5 (a) Fe K-edge HERFD-XANES spectra of eleven supported Fe catalysts and reference Fe oxides. (b) Methane partial oxidation reaction results over the eleven supported Fe catalysts. Reproduced from ref. 41 with permission from the American Chemical Society, copyright 2025.

such elements.[16,42] Although beamlines capable of performing HERFD-XANES in this high-energy range are still rare, they are expected to become increasingly important for the structural analysis of 4th-period metal catalysts. Notably, the 4th-period elements include catalytically important metals such as Rh and Pd, which are essential components of automotive exhaust purification catalysts. These metals exhibit structural changes depending on their interaction with supports and the reaction conditions, which in turn significantly affect their catalysis. By applying HERFD-XANES to structural analysis, the structural changes can be resolved with much greater resolution than achievable by conventional XANES, enabling a deeper

understanding of structure–activity relationships. An example is shown below.[25]

Rh/$\gamma$-Al$_2$O$_3$ is a highly active component of three-way automotive catalysts, but its catalytic performance deteriorates significantly under high-temperature lean (oxygen-rich) conditions. Previous studies using X-ray photoelectron spectroscopy (XPS) and Cs-STEM have suggested that this deactivation is caused by the formation of RhAlOx species. However, due to the low energy resolution of conventional XAFS, it has been difficult to distinguish RhAlO$_x$ from Rh$_2$O$_3$ in the XANES region, making it challenging to identify and quantify its presence. To overcome this limitation, Rh K-edge HERFD-XANES was applied. Fig. 6 shows the HERFD-XANES spectra of Rh/$\gamma$-Al$_2$O$_3$ before and after aging. The fresh sample exhibited spectral features similar to those of Rh$_2$O$_3$ (Fig. 3), while the aged sample showed features distinct from Rh$_2$O$_3$. These features are attributed to the formation of RhAlO$_x$. Indeed, simulated spectrum of Rh$^{3+}$ in octahedral coordination site of $\gamma$-Al$_2$O$_3$ reproduced the observed features. Therefore, octahedral RhAlOx structure was revealed to be formed in aged Rh/$\gamma$-Al$_2$O$_3$. It is important to note that conventional XANES could not differentiate between the fresh and aged samples, whereas HERFD-XANES revealed clear differences. Thus, the local structural change that was previously indistinguishable was revealed using HERFD-XANES.

### 3.3. Millisecond resolution

XAFS employing hard X-rays, which possess high material penetration capability, offers the advantage of enabling measurements under a wide range of environmental conditions. This makes it highly suitable for the *in situ* analysis of catalysts under various gas atmospheres and solutions during reactions. When combined with high-brilliance synchrotron radiation, time-resolved spectral acquisition becomes feasible through techniques such as quick-XAFS and energy-dispersive XAFS.[43,44] Recently, by integrating quick-XAFS and HERFD techniques, millisecond-resolved HERFD-XANES measurements have become possible.[45,46] Using this method, we recently succeeded in directly capturing surface reactions on a supported Pt nanoparticle catalyst.[47] Although the system introduced below involves nanoparticles rather than single atom or incorporated structures, it is presented here because time-resolved HERFD-XANES enabled a more detailed investigation of catalytic processes occurring at the active sites than was possible with conventional XANES.

The enhanced energy resolution provided by HERFD-XANES enables clearer separation of multiple components, including not only oxidized and metallic species but also molecular-adsorbed surface species.[48] This allows for the investigation of surface reactions including molecular adsorption. More specifically, whereas conventional *in situ* XANES analyses of supported metal catalysts have been largely limited to distinguishing only two components, typically metallic and oxidized states, the use of *in situ* HERFD-XANES enables more refined analyses involving three or more components, such as metallic, oxidized, and adsorbed species. Fig. 7 shows a series of millisecond-resolved *in situ* Pt L$_3$-edge HERFD-XANES spectra obtained during pulsed O$_2$ injection following CO adsorption on Pt/CeO$_2$. These spectra were successfully deconvoluted into three components: CO-adsorbed Pt nanoparticles, bare metallic Pt nanoparticles, and surface-oxidized Pt nanoparticles. The time-resolved analysis revealed that the adsorbed CO species were oxidized within 0.5 seconds after the O$_2$ pulse, leading to the formation of fully bare metallic Pt surface. Subsequently, the surface was gradually oxidized over approximately 10 seconds. Therefore, millisecond-resolved HERFD-XANES uncovered the dynamic change of the Pt nanoparticle surface, including the adsorbed state, during CO oxidation.

### 3.4. Summary of HERFD-XANES study

In Section 3, the studies on supported metal catalysts, particularly those with single-atom and incorporated structures, analyzed using HERFD-XANES spectroscopy were presented. Through HERFD-XANES, subtle differences in the coordination geometry of supported Fe complex catalysts, specifically, distortions around Fe centers in macrocyclic ligands, were elucidated and found to have a significant impact on their catalytic performance. The technique also enabled the identification of previously
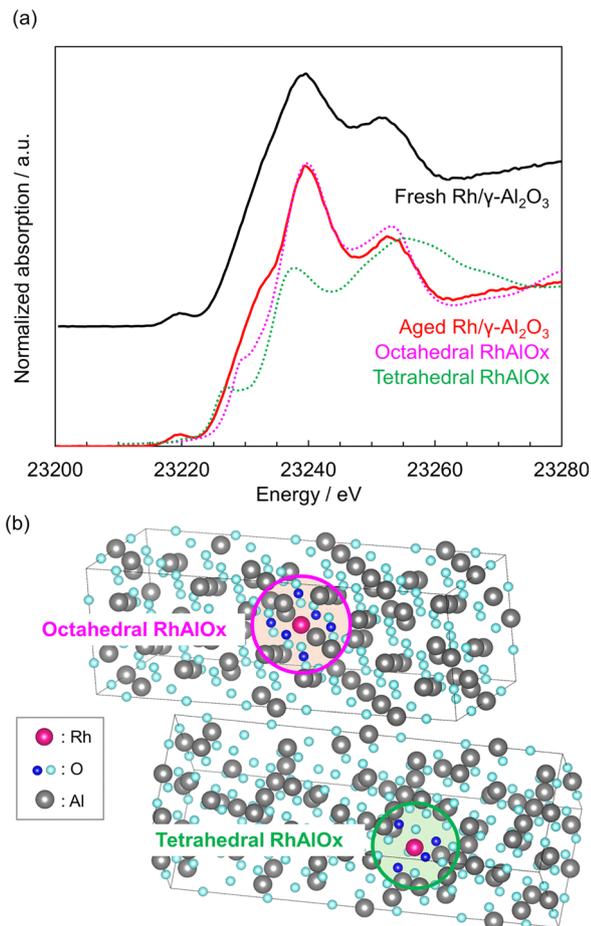


**Fig. 6** (a) Rh K-edge HERFD-XANES spectra of fresh (black solid) and aged Rh/$\gamma$-Al$_2$O$_3$ (red solid), and simulated spectra of octahedral (pink dotted) and tetrahedral RhAlO$_x$ (green dotted). (b) Structures of octahedral and tetrahedral RhAlO$_x$ species. Reproduced from ref. 25 with permission from the American Chemical Society, copyright 2025.
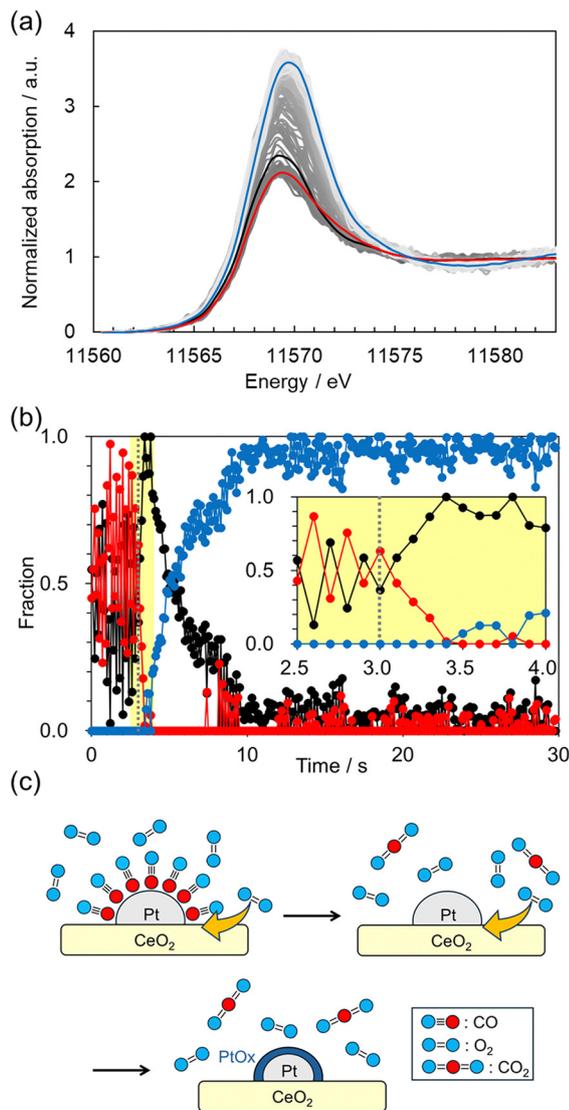
**Fig. 7** (a) Time-resolved *in situ* HERFD-XANES spectra of $Pt/CeO_2$ during the CO oxidation process with 100 ms time resolution (gray), together with static spectra of $Pt/CeO_2$ with a bare metallic Pt surface (black), CO adsorbed (red), and oxidized Pt surface (blue). (b) Time evolution of the fractions of CO-adsorbed Pt (red), bare Pt (black), and oxidized Pt (blue) during the CO oxidation process. (c) Proposed reaction mechanism of CO oxidation over $Pt/CeO_2$. Reproduced from ref. 47 with permission from the Royal Society of Chemistry, copyright 2025.

obscured structures in supported catalysts. These included the local $ABO_4$-type complex oxide structures in Fe-based catalysts for partial methane oxidation and the octahedral $RhAlO_x$ species in $Rh/\gamma$-$Al_2O_3$ for three-way catalytic reactions. Furthermore, millisecond-resolved HERFD-XANES provided a more detailed view of active-site dynamics on $Pt/CeO_2$ during CO oxidation. These results indicate that future studies using HERFD-XANES are expected to provide a clearer understanding of the structures and structure–performance relationships of active sites in supported catalysts, particularly those with highly dispersed structures such as single-atom and incorporated structures, thereby facilitating the development of new designs for such catalysts.

# 4. Cs-STEM study

Supported metal nanoparticles exhibit diverse morphologies and atomic structures that are affected by their interactions with the support and coordination environment, which result in distinctive catalytic properties. Although the atomic structures of supported metal nanoparticles were difficult to characterize using conventional methods, the advent of Cs-S/TEM has enabled their direct visualization at atomic resolution.[17–19] For such atomic-scale observations using Cs-S/TEM, high-angle annular dark-field (HAADF) STEM mode is frequently employed. In HAADF-STEM observation on a Cs-TEM, a finely focused electron beam (<0.1 nm) scans the sample area, and the electrons scattered at high angles are detected by an annular detector. The primary reason the HAADF-STEM is frequently employed is that its image interpretation is more straightforward than TEM image interpretation. For example, when observing metal nanoparticles smaller than 10 nm using TEM, the images are dominated by phase contrast, making it difficult to directly discern particle morphology.[49] In contrast, HAADF-STEM images are governed by scattering contrast, allowing more intuitive interpretation of structural features. As will be shown later, this characteristic enables 3D reconstruction *via* STEM tomography. Another advantage of HAADF-STEM is its sensitivity to atomic number (Z), which makes it easier to distinguish the supported metal species. Fig. 8(a) compares the HAADF-STEM and TEM images of Au/$\gamma$-$Al_2O_3$ taken at the same area. In the HAADF-STEM image (left image of Fig. 8(a)), Au nanoparticles appear as bright spots with
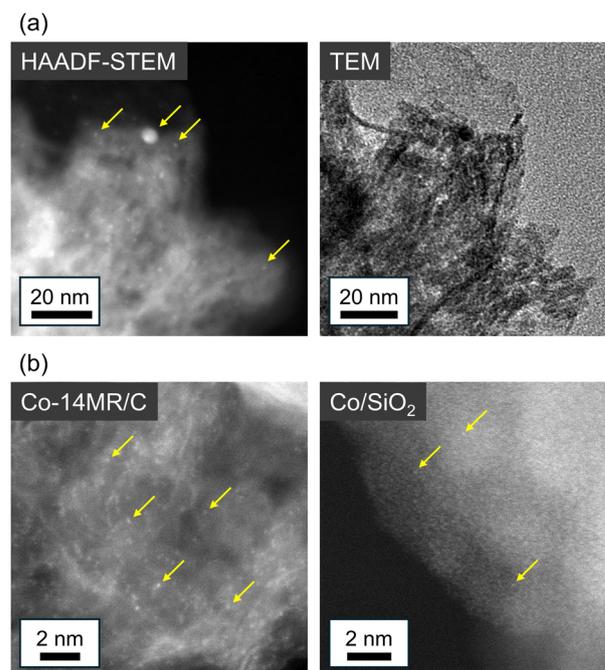


**Fig. 8** (a) Comparison of HAADF-STEM and TEM images of Au/$\gamma$-$Al_2O_3$ taken at the same area. Yellow arrows in the HAADF-STEM image indicate some Au nanoparticles. (b) Comparison of HAADF-STEM images of Co-14MR/C and Co/$SiO_2$. Yellow arrows indicate some Co single atoms. The images in (b) are reproduced from ref. 32 and 50 with permission from the American Chemical Society, copyright 2025 and 2022, respectively.

strong contrast against the $Al_2O_3$ support due to the large difference in $Z$ between Au and Al. In contrast, in the TEM image (right image of Fig. 8(a)), the Au particles appear as dark spots, but they are difficult to distinguish from the $Al_2O_3$ support. Fig. 8(b) compares HAADF-STEM images of Co-14MR/C and Co/SiO$_2$, in which Co atoms are dispersed as isolated single atoms on the supports.[32,50] On the carbon support, the Co atoms can be clearly observed, while on SiO$_2$ they are difficult to distinguish due to smaller difference in $Z$. These examples demonstrate that although the observation of single atoms can be challenging depending on the element type and combination of metal and support, Cs-STEM enables direct visualization of supported metal species at the single-atom level. In addition, the atomic arrangements within nanoparticles can also be directly observed. Accordingly, the use of Cs-STEM enables the investigation of size effects including in the sub-nanometer range as well as the influence of atomic arrangements on catalysis. Furthermore, recent advances in image processing techniques now make it possible to reconstruct 3D atomic structures.[3–11] This development enables us to understand, design, and develop catalysts from a new 3D atomic scale perspective. The following subsections present nanoparticle structures and their associated catalytic properties investigated through atomic-resolution observation.

### 4.1. From classical to non-classical structures

The size of metal nanoparticles has a significant influence on their catalytic performance. Previous studies based on idealized particle models, such as truncated-octahedral, cuboctahedral, and hemispherical particles, have demonstrated that the coordinatively unsaturated surface atoms and interfacial atoms at the metal–support boundary often play key roles in catalytic reactions. Supported Au catalysts, in particular, are well known for exhibiting pronounced size effects in oxidation and hydrogenation reactions.[1] In such systems, smaller particle sizes tend to result in higher catalytic activity due to the increased proportion of coordinatively unsaturated and interfacial surface atoms acting as active sites. This raises a simple question: does the size effect extend to the regime of single atoms and sub-2-nm clusters? To address this question, the size-dependent catalytic performance of Au/γ-$Al_2O_3$ was investigated using Cs-STEM, with particular attention given to single atoms, sub-2-nm clusters, and the active site structures (Fig. 9).[51] In this investigation, hydrogenation of two aldehydes and one nitro compound was performed. Benzaldehyde and 5-hydroxymethylfurfural were used as the aldehydes, while nitrobenzene was selected as the nitro compound. Five Au/γ-$Al_2O_3$ samples having different Au particle sizes were prepared by varying preparation temperature (Fig. 9(a)). For the size distribution analysis of Au species, image processing techniques were applied to objectively evaluate a large number of particles and obtain atomically resolved size distributions (Fig. 9(b)).[52] Furthermore, the numbers of surface local sites, *i.e.*, corner, edge, and plane sites, were quantified based on conventional cuboctahedral and truncated-octahedral models (Fig. 9(c)). The relationships between the numbers of single atoms and each surface local sites, the reaction rates, and the amounts of adsorbed reactants were carefully analyzed to investigate the active sites and size effects. As a result, it was found that isolated Au single atoms exhibited no or only low
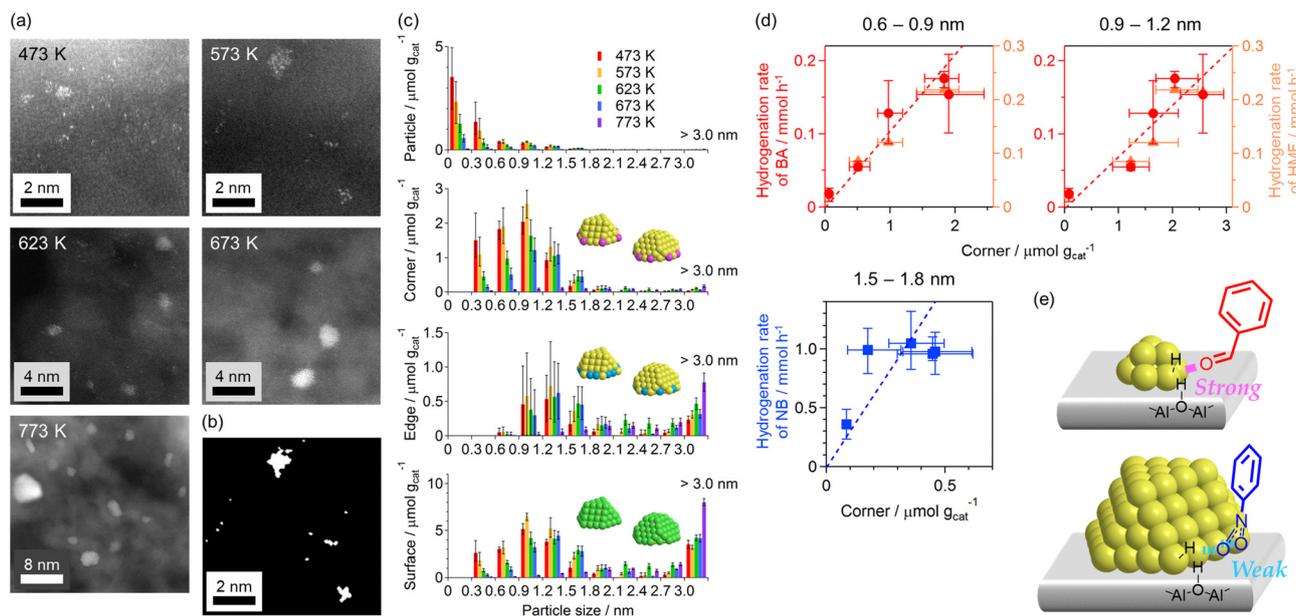


**Fig. 9** (a) HAADF–STEM images of Au/γ-$Al_2O_3$ prepared at various temperatures. (b) An example of Au clusters and atoms extracted by image processing for particle size analysis (original image: upper–right of (a)). (c) Size distributions for the number of Au particles and those for Au atoms on the corners, edges, and surface of Au clusters in a unit weight of Au/γ-$Al_2O_3$. (d) Plots of the reaction rates of benzaldehyde (BA), 5-hydroxymethylfurfural (HMF), and nitrobenzene (NB) against the number of corner atoms on Au clusters sized 0.6–0.9, 0.9–1.2, or 1.5–1.8 nm. (e) Proposed adsorption of the reactants on $Au_{10}$ and $Au_{185}$ clusters supported on γ-$Al_2O_3$: BA on a corner; NB at the interface of Au edge atoms and γ-$Al_2O_3$; $H_2$ at the interface of a Au corner and $Al_2O_3$. Reproduced from ref. 51 with permission from Elsevier, copyright 2016.

catalytic activity. Furthermore, the corner atoms of Au clusters were found to be effective reaction sites for the hydrogenation of both the aldehydes and nitrobenzene, as the dissociative adsorption of $H_2$ at the corner sites is a key step in the reaction mechanisms. Interestingly, however, the optimal cluster size differed between the two substrates. Specifically, the most effective cluster size for the aldehyde hydrogenation was 0.6–1.2 nm, whereas that for the nitrobenzene hydrogenation was 1.5–1.8 nm (Fig. 9(d)). This difference arises from their distinct adsorption behaviors: the aldehydes adsorb on corner sites, while the nitro groups adsorb on edge sites through the Au-Al$_2$O$_3$ interface (Fig. 9(e)). Therefore, the atomic-scale investigation of size effects revealed size-specific catalytic behavior in the sub-2-nm range, which arises from differences in the adsorption characteristics of functional groups.

In the case of the supported Au catalysts discussed above, the observed Au cluster structures could be interpreted using conventional structural models such as truncated-octahedra and cuboctahedra. However, in other supported catalyst systems, unconventional structures that differ from these classical models have been found. Two representative examples are presented below: one is a Ru/C catalyst for the electrochemical hydrogen oxidation reaction (HOR), and the other is a Pd/Al$_2$O$_3$ catalyst for methane combustion.[53,54]

Ru/C catalysts were developed as non-platinum catalysts for the HOR in alkaline conditions, with a focus on the size effects of Ru nanoparticles.[53] When the particle size was varied from 2 to 7 nm, the 3 nm particles exhibited notably high activity, surpassing that of conventional Pt/C catalysts (Fig. 10). To investigate the origin of this size-specific activity, the Ru nanoparticles were observed using HAADF-STEM. The 7 nm Ru particles exhibited faceted structures consistent with conventional models. In contrast, the 3 nm particles showed a more rounded morphology with disordered and distorted atomic arrangements, i.e., reduced crystallinity, and atomically rough surfaces. The 2 nm particles appeared amorphous, and additional analyses indicated that the Ru was oxidized. These findings suggest that the distinctive surface structure formed at 3 nm is responsible for the observed high activity. Interestingly, in the case of Pt/C, such reduced crystallinity is not observed even at 2 nm. This difference is likely due to the nature of the metals: Ru (a 4d metal) has less directional d orbitals compared to Pt (a 5d metal) of which 6s orbital is contracted by relativistic effects.[55] More importantly, the structures of metal nanoparticles deviate from conventional models as their size decreases. These non-classical structures, which emerge at the nanometer scale, lead to significant changes in catalytic performance.

Supported metal nanoparticles are expected to undergo structural changes depending on their interaction with the support. Focusing on this aspect, Pd/Al$_2$O$_3$ catalysts were developed for methane combustion.[54] Fig. 11 shows the size-dependent catalytic performance of Pd/Al$_2$O$_3$ for methane combustion, where three kinds of Al$_2$O$_3$ supports, e.g., γ, θ, and α-Al$_2$O$_3$, were used. The size dependence of the Pd nanoparticles strongly changed by the crystalline phase of Al$_2$O$_3$ support. HAADF-STEM observations revealed that on both θ
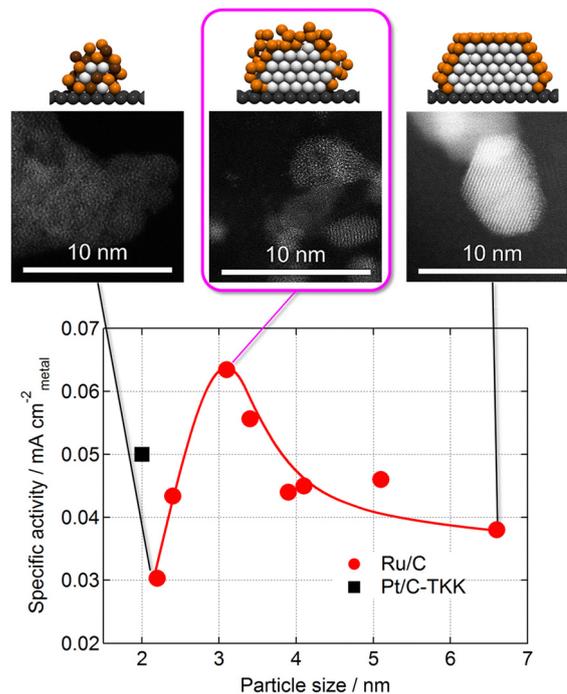


Fig. 10 Size-dependent catalytic activity of Ru/C for the alkaline HOR, along with structural variations of Ru nanoparticles with their size. Reproduced from ref. 53 with permission from the American Chemical Society, copyright 2013.

and α-Al$_2$O$_3$, Pd nanoparticles exhibited faceted structures at 20 nm. However, when the particle size decreased to 5–10 nm, the atomic arrangement became disordered and the particles adopted a more rounded morphology. At 2 nm, the atomic structure was further disordered, and the particles exhibited highly distorted shapes. Therefore, the spherical 5–10 nm Pd nanoparticles with stepped surfaces were suggested to be highly active for methane combustion, while the faceted large Pd nanoparticles or the amorphous-like small Pd nanoparticles were less active. In contrast to Pd nanoparticles supported on θ and α-Al$_2$O$_3$, those on γ-Al$_2$O$_3$ exhibited distorted shapes even at 20 nm. This is attributed to the presence of penta-coordinate Al$^{3+}$ sites in γ-Al$_2$O$_3$ strongly interacting with the Pd nanoparticles. Thus, the strong Pd-γ-Al$_2$O$_3$ interaction retained the distorted shapes of Pd nanoparticles even at larger particle sizes, resulting in only a modest increase in catalytic activity with increasing particle size. These findings demonstrate that the metal–support interaction alters the structure of supported metal nanoparticles, which in turn changes the size dependence of catalytic activity.

### 4.3. 3D structure

As shown above, the use of Cs-STEM has enabled atomic-resolution visualization of supported metal nanoparticle structures, making it possible to analyze size effects in the sub-2-nm range, as well as the impact of non-classical structure formation. However, detailed information on the morphology and the surface and internal disorder of supported metal
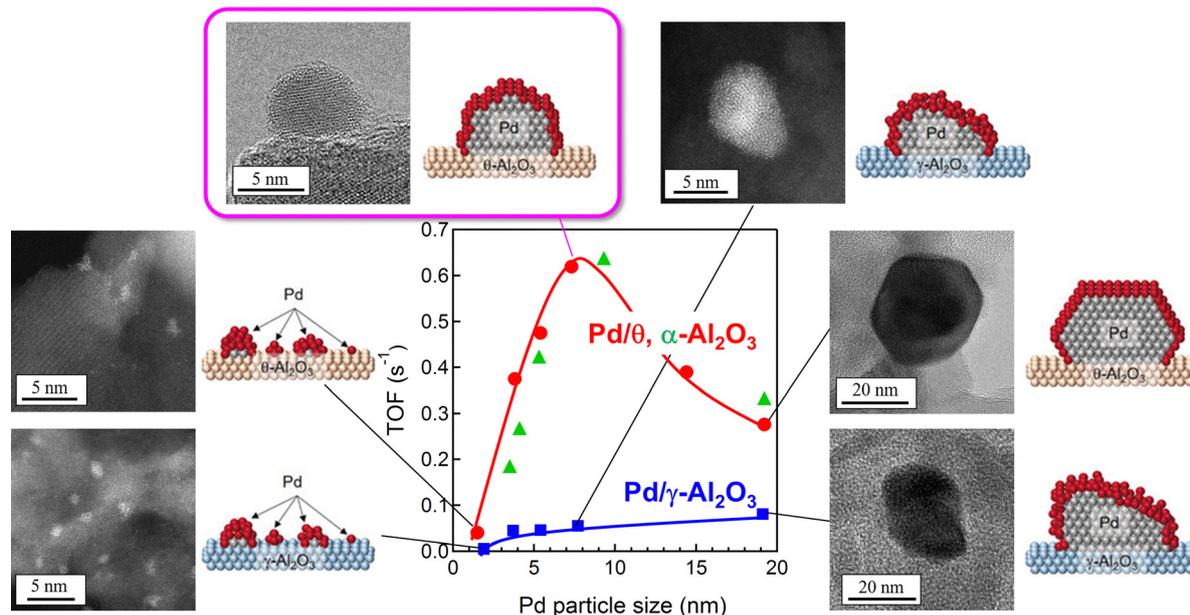
**Fig. 11** Size- and support-dependent catalytic activity of Pd/Al$_2$O$_3$ for methane combustion, along with structural variations of Pd nanoparticles with their size and support. Reproduced from ref. 54 with permission from Wiley-VCH, copyright 2017.

nanoparticles still remains elusive. To investigate these features, it is necessary to examine the 3D structure of catalysts. Since HAADF-STEM images are based primarily on scattering contrast, morphological information is inherently present in the images; however, it is difficult to fully understand the 3D structure of nanoparticles from images taken from a single projection direction. Tomographic techniques are therefore required to reconstruct their 3D structure.

Recent advances in software have made it relatively easy to perform electron tomography at the nanometer scale. Using the latest software, a series of tilted HAADF-STEM images can be acquired semi-automatically and reconstructed into a 3D image with nanometer-scale space resolution (not in atomic resolution).[56] This technique was applied to investigate the effect of the support effect of Ni/C developed as non-platinum catalysts for the HOR.[57] Fig. 12(a) shows the results of 3D structural analysis of Ni nanoparticles supported on two different carbon powder: Ketjenblack (C$_K$) and Vulcan XC-72R (C$_V$) (corresponding movies are provided in ref. 57). Using the TEMography software, a series of tilted STEM images was acquired over angular ranges of −50 to 60° and −64 to 68°, and a 3D image was reconstructed. Based on differences in signal intensity of Ni and carbon, color mapping was applied, with red corresponding to Ni nanoparticles and green to the carbon supports. The Ni particles supported on C$_K$ exhibited angular shapes with flat surfaces, whereas those on C$_V$ displayed more rounded morphologies. XPS analysis of the carbon supports indicated that C$_K$ contains a lower proportion of oxidized carbon and a higher proportion of graphitic carbon compared to C$_V$. These results suggest that the interaction between Ni nanoparticles and graphitic carbon leads to the formation of angular particle shapes. Fig. 12(b) compares the surface-area specific catalytic activity of Ni/C$_K$ and Ni/C$_V$ for
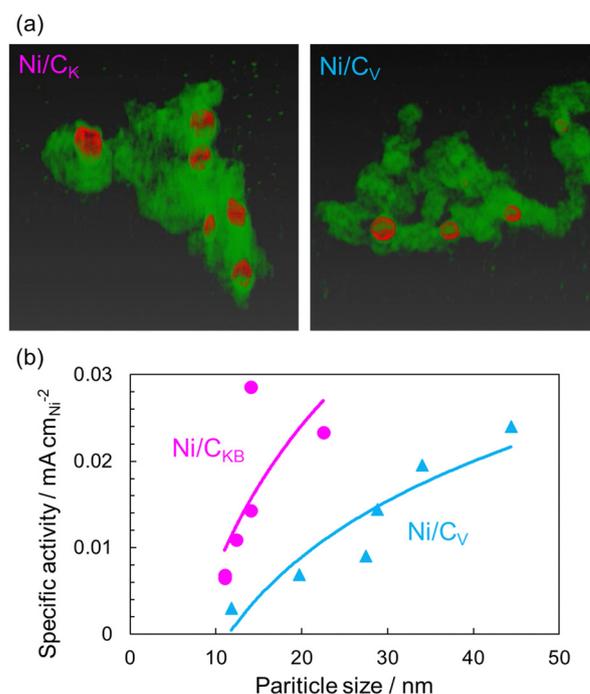


**Fig. 12** (a) Representative views of the 3D structures of Ni/C$_K$ and Ni/C$_V$. Red: Ni; green: C. (b) Difference of catalytic activity between Ni/C$_K$ and Ni/C$_V$ for the alkaline HOR. Reproduced from ref. 57 under a CC-BY-NC license. Published by the American Chemical Society.

the HOR. Ni/C$_K$ exhibited significantly higher activity than Ni/C$_V$. Therefore, the nanometer-scale 3D structure analysis demonstrated that the differences in nanoparticle morphology and surface structure arising from metal–support interactions strongly affect the catalytic activity.

In order to investigate surface structures of supported metal nanoparticles in greater detail, atomic-resolution 3D structural analysis is required. Such 3D atomic structure analysis has been made possible only recently by advances in Cs-STEM and tomography.[3–11] Applying this technique to supported metal catalysts can make it possible to elucidate atomic structures and structure–performance relationships that were beyond reach until now. To demonstrate this, atomic-resolution 3D structural analysis was performed on the Pd/θ-Al$_2$O$_3$ which exhibited high activity for methane combustion (Fig. 11).[3] While 3D atomic structural analysis of a supported Pd nanoparticle was carried out based on a 73 tilt series images, the non-uniform background signal from the θ-Al$_2$O$_3$ support hindered an accurate 3D reconstruction. To obtain an accurate atomic structure of the Pd nanoparticle, it was necessary to isolate only the signal corresponding to the Pd nanoparticle by removing the non-uniform background from the θ-Al$_2$O$_3$ support. Two approaches can be considered for the signal extraction. One involves reconstructing the 3D structure including both Pd and θ-Al$_2$O$_3$, followed by extraction of the Pd nanoparticle from the reconstructed volume. The other approach involves isolating the Pd signal in advance directly from the HAADF-STEM images prior to reconstruction. In the present analysis of Pd/θ-Al$_2$O$_3$, the latter approach was adopted. Since it was difficult to simulate the complex background from the θ-Al$_2$O$_3$ support using mathematical functions, a deep learning-based inpainting technique was employed. Specifically, a convolutional neural network (CNN) was trained using 558 HAADF-STEM images of the θ-Al$_2$O$_3$ support. Using the trained model, inpainted images of the Pd region, i.e. θ-Al$_2$O$_3$ background images, were generated. These background images were then subtracted from the original images to isolate the Pd nanoparticle signal (Fig. 13(a)). This processing was applied to all 73 tilt-angle images, and the resulting Pd-only images were used to reconstruct the 3D structure (Fig. 13(b)). Finally, the positions of individual Pd atoms were determined from the image intensities to obtain the 3D atomic structure (a movie showing the 3D atomic structure is available in ref. 3). The view of the 3D atomic structure along ⟨101⟩ is shown in Fig. 13(c). Note that once the 3D atomic structure is reconstructed, the nanoparticle can be evaluated from all directions, leading to elucidation of its crystal structure, morphology, and surface characteristics. Consequently, the particle was revealed to have a disordered face-centered cubic (FCC) lattice. Accompanying this lattice disorder, the particle adopted a distorted and rounded morphology resembling a truncated octahedron. The surface displayed disordered {111} and {100} facets. Additionally, and of particular interest, high-index {212} facets were also observed. These disordered and high-index facets are attributed to the reason for the high catalytic activity of the Pd/θ-Al$_2$O$_3$ catalyst in methane combustion (Fig. 11). Therefore, based on the 3D atomic structure of Pd nanoparticle, the structural features responsible for the extraordinary catalytic activity of Pd/θ-Al$_2$O$_3$ were identified. Notably, this study represents the first example of visualizing the 3D atomic structure of practical metal nanoparticles supported on a metal oxide.
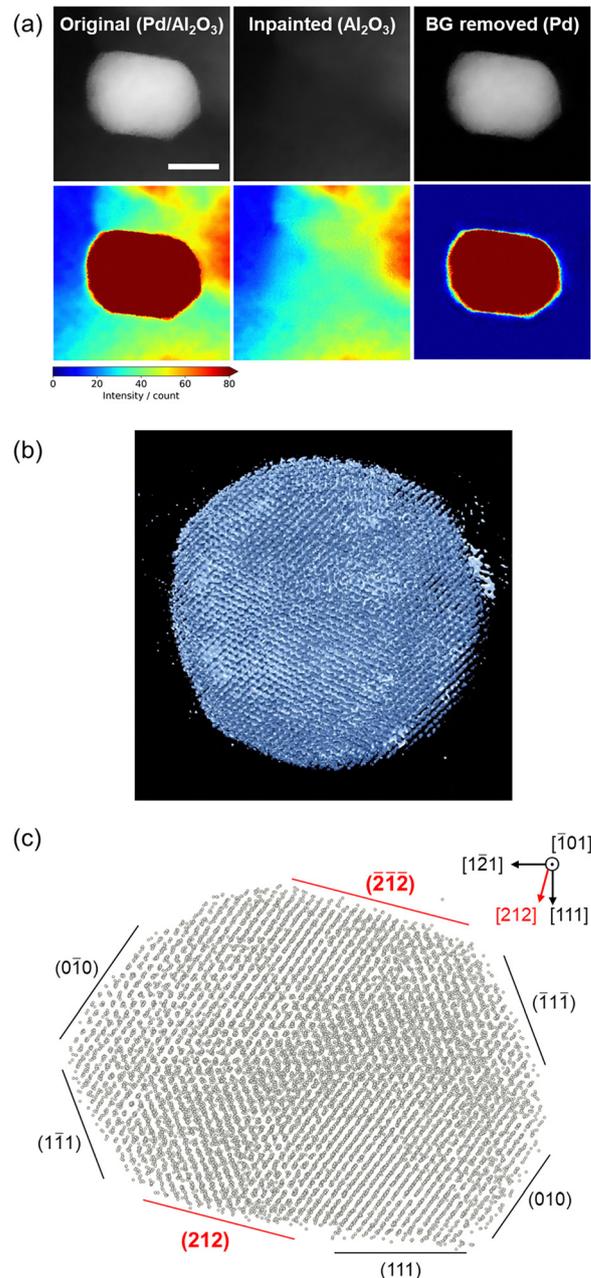


Fig. 13 (a) A HAAFD-STEM image of Pd/θ-Al$_2$O$_3$ before and after CNN-based inpainting and background (BG) subtraction. Top: Grayscale; Bottom: Heat map. (b) 3D reconstructed Pd nanoparticle. (c) View of the 3D atomic structure of Pd nanoparticle along ⟨101⟩ direction. Reproduced form ref. 3 with permission from Wiley–VCH, copyright 2024.

### 4.4. Summary of Cs-STEM studies

In Section 4, the studies on supported metal nanoparticle catalysts investigated using Cs-STEM were presented. The atomic-resolution imaging capability of Cs-STEM enabled us to elucidate the size-dependent catalytic performance of Au/γ-Al$_2$O$_3$ in the hydrogenation reactions, particularly in the sub-2 nm range. Moreover, the formation of non-classical metal nanoparticle structures in Ru/C and Pd/Al$_2$O$_3$, induced by particle size and metal–support

interactions, was identified. These non-classical structures were found to exhibit distinctive catalytic properties for the HOR and methane combustion, respectively. Furthermore, the 3D atomic structure of a Pd nanoparticle supported on $\theta$-$Al_2O_3$ having high activity for methane combustion was visualized, which led to the direct identification of actual particle morphology and active surface structures with atomic resolution. This 3D atomic-scale structural analysis may represent a paradigm shift in supported metal catalyst study, as it provides deeper and clearer insights into surface active sites and their local structures, offering a foundation for the rational design of next-generation catalysts.

## 5. Outlook and perspectives

Conventionally, reaction mechanisms on solid catalysts have been discussed based on structural models inferred from spatially averaged spectroscopic data. Computational chemistry then has allowed validation of these models. In parallel, advances in electron microscopy have enabled direct atomic-scale observation of solid catalysts, leading to more realistic and evidence-based discussions of catalyst structures. Today, rapid progress in digital technologies is further enhancing researchers' ability to analyze catalysts at the atomic level. The integration of these technologies with ongoing advanced analytical methods is now enabling 3D atomic structure analysis of practical supported metal catalysts, providing a foundation for catalyst understanding and development based on experimentally observed structures rather than assumed model structures. As demonstrated by the recent works presented herein, even the complex and heterogeneous structures of practical supported metal catalysts can now be analyzed at the atomic level. Driven by such advances, heterogeneous catalyst research is expected to shift in the future from being based on hypothetical models to being based on experimentally observed 3D atomic structures. Moreover, it is worth noting that the reconstruction of 3D atomic structures enables their digital representation. Accordingly, 3D atomic structure analysis of supported metal nanoparticles opens the door to building structural databases of practical nanoparticle catalysts. The continued advancement of 3D atomic structure analyses of supported catalysts will accelerate the understanding of structure–performance relationships and promote data-driven catalyst design and discovery.

## Conflicts of interest

There are no conflicts to declare.

## Data availability

No primary research results, software or code have been included and no new data were generated or analysed as part of this review.

## Acknowledgements

## Notes and references

1 T. Takei, T. Akita, I. Nakamura, T. Fujitani, M. Okumura, K. Okazaki, J. Huang, T. Ishida and M. Haruta, in *Advances in Catalysis*, ed. B. C. Gates and F. C. Jentoft, Academic Press, 2012, vol. 55, pp. 1–126.
2 G. A. Somorjai and J. Y. Park, *Angew. Chem., Int. Ed.*, 2008, **47**, 9212–9228.
3 H. Iwai, F. Nishino, T. Yamamoto, M. Kudo, M. Tsushida, H. Yoshida, M. Machida and J. Ohyama, *Small Methods*, 2024, **8**, 2301163.
4 Y. Yang, J. Zhou, Z. Zhao, G. Sun, S. Moniri, C. Ophus, Y. Yang, Z. Wei, Y. Yuan, C. Zhu, Y. Liu, Q. Sun, Q. Jia, H. Heinz, J. Ciston, P. Ercius, P. Sautet, Y. Huang and J. Miao, *Nat. Catal.*, 2024, **7**, 796–806.
5 H. Jo, D. H. Wi, T. Lee, Y. Kwon, C. Jeong, J. Lee, H. Baik, A. J. Pattison, W. Theis, C. Ophus, P. Ercius, Y.-L. Lee, S. Ryu, S. W. Han and Y. Yang, *Nat. Commun.*, 2022, **13**, 5957.
6 X. Tian, X. Yan, G. Varnavides, Y. Yuan, D. S. Kim, C. J. Ciccarino, P. Anikeeva, M.-Y. Li, L.-J. Li, P. Narang, X. Pan and J. Miao, *Sci. Adv.*, 2021, **7**, eabi6699.
7 J. Lee, C. Jeong and Y. Yang, *Nat. Commun.*, 2021, **12**, 1962.
8 J. Lee, C. Jeong, T. Lee, S. Ryu and Y. Yang, *Nano Lett.*, 2022, **22**, 665–672.
9 Y. Yang, J. Zhou, F. Zhu, Y. Yuan, D. J. Chang, D. S. Kim, M. Pham, A. Rana, X. Tian, Y. Yao, S. J. Osher, A. K. Schmid, L. Hu, P. Ercius and J. Miao, *Nature*, 2021, **592**, 60–64.
10 Y. Yang, C.-C. Chen, M. C. Scott, C. Ophus, R. Xu, A. Pryor, L. Wu, F. Sun, W. Theis, J. Zhou, M. Eisenbach, P. R. C. Kent, R. F. Sabirianov, H. Zeng, P. Ercius and J. Miao, *Nature*, 2017, **542**, 75–79.
11 A. Pryor, Y. Yang, A. Rana, M. Gallagher-Jones, J. Zhou, Y. H. Lo, G. Melinte, W. Chiu, J. A. Rodriguez and J. Miao, *Sci. Rep.*, 2017, **7**, 10409.
12 M. A. Newton, A. J. Knorpp, V. L. Sushkevich, D. Palagin and J. A. van Bokhoven, *Chem. Soc. Rev.*, 2020, **49**, 1449–1486.
13 P. Glatzel, M. Sikora, G. Smolentsev and M. Fernández-García, *Catal. Today*, 2009, **145**, 294–299.
14 G. E. Cutsail Iii and S. DeBeer, *ACS Catal.*, 2022, **12**, 5864–5886.
15 H. Asakura and T. Tanaka, *Chem. Lett.*, 2021, **50**, 1075–1085.
16 N. Hiraoka, *J. Synchrotron Radiat.*, 2025, **32**, 109–117.
17 A. A. Herzing, C. J. Kiely, A. F. Carley, P. Landon and G. J. Hutchings, *Science*, 2008, **321**, 1331–1335.
18 S. N. Rashkeev, A. R. Lupini, S. H. Overbury, S. J. Pennycook and S. T. Pantelides, *Phys. Rev. B:Condens. Matter Mater. Phys.*, 2007, **76**, 035438.
19 A. Uzun, V. Ortalan, Y. Hao, N. D. Browning and B. C. Gates, *ACS Nano*, 2009, **3**, 3691–3695.
20 A. Bergmann and B. Roldan Cuenya, *ACS Catal.*, 2019, **9**, 10020–10043.
21 T. Li, A. J. Senesi and B. Lee, *Chem. Rev.*, 2016, **116**, 11128–11180.
22 F. Herrera, G. Rumi, P. Y. Steinberg, A. Wolosiuk and P. C. Angelomé, *ChemCatChem*, 2023, **15**, e202300490.
23 J. Ohyama, M. Moriya, R. Takahama, K. Kamoi, S. Kawashima, R. Kojima, T. Hayakawa and Y. Nabae, *JACS Au*, 2021, **1**, 1798–1804.
24 Z. Feng, S. Honda, J. Ohyama, Y. Iwata, K. Awaya, H. Yoshida, M. Machida, K. Higashi, T. Uruga, N. Kawamura, R. Goto, T. Ichihara, R. Kojima, M. Moriya, H. Notsu, S. Nagata, M. Miyoshi, T. Hayakawa and Y. Nabae, *ACS Catal.*, 2024, **14**, 7416–7425.
25 M. Sato, K. Awaya, M. Tsushida, M. Machida, N. Hiraoka and J. Ohyama, *ACS Catal.*, 2025, **15**, 6466–6472.
26 T. Matsumoto, K. Nakada, T. Matsushita, S. Yokota, Y. Furukawa, A. Yamashita and M. Kodera, *AIP Conf. Proc.*, 2019, **2054**.
27 E. Proietti, F. Jaouen, M. Lefèvre, N. Larouche, J. Tian, J. Herranz and J.-P. Dodelet, *Nat. Commun.*, 2011, **2**, 416.
28 Y. Nabae, S. Nagata, T. Hayakawa, H. Niwa, Y. Harada, M. Oshima, A. Isoda, A. Matsunaga, K. Tanaka and T. Aoki, *Sci. Rep.*, 2016, **6**, 23276.
29 Y. Nabae, S. Nagata, K. Kusaba, T. Aoki, T. Hayakawa, H. Tanida, H. Imai, K. Hori, Y. Yamamoto, S. Arai and J. Ohyama, *Catal. Sci. Technol.*, 2020, **10**, 493–501.

30 J. Li, M. T. Sougrati, A. Zitolo, J. M. Ablett, I. C. Oğuz, T. Mineva, I. Matanovic, P. Atanassov, Y. Huang, I. Zenyuk, A. Di Cicco, K. Kumar, L. Dubau, F. Maillard, G. Dražić and F. Jaouen, *Nat. Catal.*, 2021, **4**, 10–19.

31 M. Moriya, R. Takahama, K. Kamoi, J. Ohyama, S. Kawashima, R. Kojima, M. Okada, T. Hayakawa and Y. Nabae, *J. Phys. Chem. C*, 2020, **124**, 20730–20735.

32 Z. Feng, J. Ohyama, S. Honda, Y. Iwata, K. Awaya, M. Machida, M. Tsushida, R. Goto, T. Ichihara, M. Moriya and Y. Nabae, *J. Am. Chem. Soc.*, 2025, **147**, 15377–15388.

33 A. Hirayama, Y. Tsuchimura, H. Yoshida, M. Machida, S. Nishimura, K. Kato, K. Takahashi and J. Ohyama, *Catal. Sci. Technol.*, 2021, **11**, 6217–6224.

34 J. Ohyama, A. Hirayama, Y. Tsuchimura, N. Kondou, H. Yoshida, M. Machida, S. Nishimura, K. Kato, I. Miyazato and K. Takahashi, *Catal. Sci. Technol.*, 2021, **11**, 3437–3446.

35 J. Ohyama, A. Hirayama, H. Yoshida, M. Machida, K. Kato, S. Nishimura and K. Takahashi, *J. Jpn. Pet. Inst.*, 2023, **66**, 180–184.

36 J. Ohyama, Y. Tsuchimura, A. Hirayama, H. Iwai, H. Yoshida, M. Machida, S. Nishimura, K. Kato and K. Takahashi, *ACS Catal.*, 2022, **12**, 2454–2462.

37 Y. Tsuchimura, H. Yoshida, M. Machida, S. Nishimura, K. Takahashi and J. Ohyama, *Energy Fuels*, 2023, **37**, 9411–9418.

38 T. Akiyama, R. Sei and S. Takenaka, *Catal. Sci. Technol.*, 2021, **11**, 5273–5281.

39 A. Matsuda, T. Aihara, S. Kiyohara, Y. Kumagai, M. Hara and K. Kamata, *ACS Appl. Nano Mater.*, 2024, **7**, 10155–10167.

40 J. Ohyama, H. Iwai, D. Takahashi, M. Tsushida, M. Machida, S. Nishimura and K. Takahashi, *ChemCatChem*, 2024, e202401045.

41 J. Ohyama, Y. Yoshioka, M. Tsukamoto, R. Kuroki, D. Takahashi, K. Awaya, M. Machida, K. Higashi, T. Uruga, N. Kawamura, S. Nishimura and K. Takahashi, *ACS Catal.*, 2025, **15**, 697–705.

42 R. Bjornsson, F. A. Lima, T. Spatzal, T. Weyhermüller, P. Glatzel, E. Bill, O. Einsle, F. Neese and S. DeBeer, *Chem. Sci.*, 2014, **5**, 3096–3103.

43 J. Ohyama, K. Teramura, Y. Higuchi, T. Shishido, Y. Hitomi, K. Kato, H. Tanida, T. Uruga and T. Tanaka, *ChemPhysChem*, 2011, **12**, 127–131.

44 Y. Mahara, K. Murata, K. Ueda, J. Ohyama, K. Kato and A. Satsuma, *ChemCatChem*, 2018, **10**, 3384–3387.

45 K. Higashi, S. Takao, G. Samjeské, H. Matsui, M. Tada, T. Uruga and Y. Iwasawa, *Phys. Chem. Chem. Phys.*, 2020, **22**, 18919–18931.

46 T. Uruga, M. Tada, O. Sekizawa, Y. Takagi, T. Yokoyama and Y. Iwasawa, *Chem. Rec.*, 2019, **19**, 1444–1456.

47 J. Ohyama, M. Sato, M. Tsushida, K. Awaya, M. Machida, T. Uruga and K. Higashi, *Catal. Sci. Technol.*, 2025, **15**, 2544–2550.

48 M. K. Oudenhuijzen, J. A. van Bokhoven, J. T. Miller, D. E. Ramaker and D. C. Koningsberger, *J. Am. Chem. Soc.*, 2005, **127**, 1530–1540.

49 N. Tanaka, *Electron Nano-imaging: Basics of Imaging and Diffraction for TEM and STEM*, 2017.

50 J. Ohyama, D. Abe, A. Hirayama, H. Iwai, Y. Tsuchimura, K. Sakamoto, M. Irikura, Y. Nakamura, H. Yoshida, M. Machida, S. Nishimura, T. Yamamoto, S. Matsumura and K. Takahashi, *J. Phys. Chem. C*, 2022, **126**, 1785–1792.

51 J. Ohyama, A. Esaki, T. Koketsu, Y. Yamamoto, S. Arai and A. Satsuma, *J. Catal.*, 2016, **335**, 24–35.

52 Y. Yamamoto, S. Arai, A. Esaki, J. Ohyama, A. Satsuma and N. Tanaka, *Microscopy*, 2014, **63**, 209–218.

53 J. Ohyama, T. Sato, Y. Yamamoto, S. Arai and A. Satsuma, *J. Am. Chem. Soc.*, 2013, **135**, 8016–8021.

54 K. Murata, Y. Mahara, J. Ohyama, Y. Yamamoto, S. Arai and A. Satsuma, *Angew. Chem., Int. Ed.*, 2017, **56**, 15993–15997.

55 S. I. Sanchez, M. W. Small, E. S. Bozin, J.-G. Wen, J.-M. Zuo and R. G. Nuzzo, *ACS Nano*, 2013, **7**, 1542–1557.

56 H. Kudo, D. Jian, K. Kamo, N. Horii, H. Furukawa, S. Hata, M. Murayama, K. Sato and S. Miyazaki, *Kenbikyo*, 2016, **51**, 48–53.

57 Y. Akamine, F. Nishino, T. Yamashita, M. Tsushida, K. Awaya, M. Machida, S. M. Zahan, D. R. Dekel and J. Ohyama, *ACS Appl. Mater. Interfaces*, 2024, **16**, 69316–69323.